



LAWRENCE  
LIVERMORE  
NATIONAL  
LABORATORY

# Feasibility Study of a Passive, Standoff Detector of High Density Masses with a Gravity Gradiometer Based on Atom Interferometry

S. B. Libby, V. Sonnad, S. A. Kreek, K. W. Brady, M. R.  
Matthews, B. Dubetsky, A. Vitouchkine, B. C. Young

January 14, 2011

This document was prepared as an account of work sponsored by an agency of the United States government. Neither the United States government nor Lawrence Livermore National Security, LLC, nor any of their employees makes any warranty, expressed or implied, or assumes any legal liability or responsibility for the accuracy, completeness, or usefulness of any information, apparatus, product, or process disclosed, or represents that its use would not infringe privately owned rights. Reference herein to any specific commercial product, process, or service by trade name, trademark, manufacturer, or otherwise does not necessarily constitute or imply its endorsement, recommendation, or favoring by the United States government or Lawrence Livermore National Security, LLC. The views and opinions of authors expressed herein do not necessarily state or reflect those of the United States government, Department of Defense or Lawrence Livermore National Security, LLC, and shall not be used for advertising or product endorsement purposes.

This work performed under the auspices of the U.S. Department of Energy by Lawrence Livermore National Laboratory under Contract DE-AC52-07NA27344.

**Final Report LDRD 10-FS-003:**

Feasibility Study of a Passive, Stand-off Detector of High-Density Masses with a Gravity Gradiometer Based on Atom Interferometry

Stephen B. Libby, Vijay Sonnad, Steven A. Kreek  
Lawrence Livermore National Laboratory, Livermore, CA 94550

Kyle W. Brady  
U. C. Berkeley & Lawrence Livermore National Laboratory

Michael R. Matthews, Boris Dubetsky, Artyom Vitouchine, Brenton C. Young  
AOSense Inc., 767 N Mary Ave., Sunnyvale, CA 94085

**Executive Summary:**

For the emergency response (ER) and treaty verification communities, methods to determine and/or verify the masses present in containers are highly desirable. Additionally, the ability to perform these measurements passively and rapidly is also important in the ER community. The ability to quantify relevant masses and aspects of their spatial distribution is essential for setting lower bounds in relevant ER calculations and for monitoring treaty compliance. The purpose of this feasibility study was to demonstrate a completely passive, rapid method to determine the mass of high-density material present in a closed box, without the need to move, radiograph, or otherwise manipulate the box. Our method applies an existing, DARPA-AOSense, Inc. developed gravity gradiometer based on atomic fountain interferometer technology originally invented by Steven Chu and his team at Stanford, to perform differential gravity measurements, taken from positions around the container with the heavy mass sources inside. In this feasibility study, done with the AOSense gradiometer, we (equivalently) carried out the measurements by moving the mass source, in the required arrangements and orientations, parallel to the atomic fountain axis. We also built and applied computational models of the atomic fountain responses to our high-density mass sources and the background container to enable the blind determination of the overall masses and configurations of material present in the container in our experiments.

Specifically, in this feasibility study demonstration, we successfully used the existing gradiometer at AOSense, Inc. developed for DARPA, to detect masses and multi-polar aspects of their distribution as a function of distance and integration time with high accuracy. Typical situations involved the detection, to within a few percent, of pairs of 12.7 kg. tungsten cylindrical masses in various configurations between 0.3 m and 0.8 m from the instrument axis. Our computational models, including time series signal analysis of the atomic fountain response, based on potential theory and a semi-classical approximation of the atomic phase shifts, matched the experimental data well. Furthermore, we carried out a detailed noise (Allan deviation) analysis of the fountain interferometer phase noise as well as background measurements of an empty box. These models, as well as signal analysis, noise, and background results will form the basis of

future hypothesis test models for rapid gravity gradient mass detection and analysis with instruments of this type.

Having successfully demonstrated the potential of cold atom interferometers to rapidly and passively image mass distributions, we now seek to develop and execute proposals to design, construct and field a portable system (including developing the required modeling and analysis software) for use by the ER and treaty verification communities. This has the potential to replace aspects of x-ray radiography with a completely passive technique.

### **Technical Basis for the Work:**

High-density components can, in principle, be detected by their effect on the local gravitational field. This fact motivated our adoption<sup>11</sup> of an advanced version of the gravity gradiometer sensor developed and demonstrated by AOSense, Inc. for DARPA (see Figure 1). This type of gradiometer, based on very well established atomic source laser cooling and trapping (magneto-optical trap and/or optical molasses), and a separate laser-driven light-pulse atom (LPA) interferometer consisting of a beam splitter, combiner, and phase read out, was initially used in 2002 to measure gravitational gradients due to  $\sim 100$  kg perturbing masses at distances of  $\sim 0.2$  m, corresponding to an acceleration of  $\sim 8 \times 10^{-9} g$ . (Kasevich and Chu, '92, McGuirk et al. '02).<sup>1</sup>

Precise gravity measurements using mechanical instruments (modern examples being torsion pendulums and balances, falling corner cubes, and superconducting accelerometers)<sup>14-18</sup> of local gravitational field variations due to nearby perturbing masses go back at least to Bouger, Cavendish and Eötvös. Early applications were to geodesy. More recently, very sensitive torsion balances and superconducting gravimeters and gradiometers have been applied to fundamental physics with the goal of discovering, or at least setting bounds on non-Newtonian, mass coupled, static short distance forces that might arise as a consequence of grand unification.<sup>19</sup> However, these instruments are ill-suited to mobile, rapid data acquisition because of their mechanical calibration requirements<sup>14-16</sup> and general lack of long-term stability. In contrast, the cold atom interferometer gravity gradiometer used in this study and proposed for ER and treaty verification mobile applications, only depends on fundamental atomic physics, has no cryogenic requirements, has been demonstrated to be stable for long periods, and has the potential for significant miniaturization.<sup>1,6,8,12</sup>

Recent significant improvements in this technology combined with the contribution of LLNL's advanced computation and knowledge of ER requirements, led us to believe it possible to design and develop a portable gradiometer system that is capable of measuring, in minutes, masses relevant to the ER and treaty verification communities. The exact detection limits (SNR) at different distances depends upon the noise<sup>7</sup> sensitivity scaling, which was one of the subjects of this feasibility study. In addition to the present gradiometer's unique passive mass detection capability, mass imaging by moving the detectors to acquire phase shifts from different positions (as done in this study) or by use of multiple sensors, combined with future improvements in noise reduction and the exploitation of quantum coherence will likely yield even greater sensor performance.

## State of technology and scientific basis:

### *Light-Pulse Atom (LPA) sensors overview*

The discovery of laser cooling of neutral atoms, which enabled applications of ultra slow atoms ( $T \sim 10^{-6}$  K), dates back to the mid 1980's (Steven Chu, Claude Cohen-Tannoudji, William Phillips, Nobel Prize 1997).<sup>9</sup> In particular, atom interferometric sensors, based on laser-cooled sources, exploit the wavelike properties of atoms to achieve unparalleled accuracies orders-of-magnitude superior to conventional sensors. The light-pulse atom (LPA) interference method (the method applied in the gravity gradiometer in this proposal) uses successive interactions with laser beams to measure an atom's inertial trajectory (and therefore phase) with respect to an optical reference mirror fixed relative to the sensor case. In this respect, the atom interferometer is a quantum analog of the classical wave Mach-Zehnder interferometer widely applied in optics.<sup>1,2,4</sup>

Here, the laser beam frequencies are resonant with a transition between two of the atom's internal quantum states. Under appropriate conditions, the atom records the phase of the driving electromagnetic field during each resonant interaction. This phase is directly proportional to the distance of the atom from the optical reference mirror that defines the laser field phase (*i.e.*,  $\phi = \mathbf{k} \cdot \mathbf{x}$ , where  $\mathbf{k}$  is the propagation vector of the interrogating laser and  $\mathbf{x}$  is the distance of the atom from the reference mirror). Key features of the light-pulse approach are: (i) *No coupling of the sensor proof-mass to sensor case.* Atoms are in a high to ultra-high vacuum environment, in a quantum state that is immune to external electromagnetic fields. (ii) *High accuracy pick-off.* A frequency-stabilized laser measures the relative motion between the proof mass and case. (iii) *Conceptual simplicity.* A complete sensor requires a laser source, vacuum cell, atomic vapor and control electronics. In contrast to its mechanical sensor competitors, there are no moving parts (other than the atomic proof mass). Attributes (i) and (ii) enable exceptionally accurate sensors. Attribute (iii) indicates that after appropriate engineering refinements, these sensors should be robust and cost-effective to manufacture and maintain. In the laboratory, LPA sensors have precisely measured rotations,<sup>2</sup> gravitational acceleration and gravity gradients,<sup>1</sup> the Newtonian gravitational constant,<sup>3</sup> and the fine structure constant.<sup>4</sup> Now LPA sensors are transitioning from the laboratory to field applications.<sup>5</sup> The AOSense team and their closely coupled Stanford collaborators are world leaders in this field, having led the way in both basic and applied uses of laser-pulsed atom interferometry for many years.

In practical LPA sensors, lasers cool a cloud of atoms and launch or drop them as required. Additional microwave and/or optical pulses prepare the atoms in a known state, and a series of three (or more) Raman pulses create the atom interferometer. Resonant fluorescence detection measures the excitation probability  $P_e$  that an atom ends up in a particular ground state after the interferometer sequence:  $P_e = [1 - \cos(\Delta\Phi + \phi_L)] / 2$ . Here  $\Delta\Phi = \phi_1 - 2\phi_2 + \phi_3$  is the net phase difference between two paths of the interferometer, and  $\phi_L$  is due to the laser arbitrary phase.  $\phi_i = \vec{k}_i \cdot \vec{x}_i$  is the phase shift the atoms acquire due to momentum transfer from Raman pulse  $i$  when the atoms are at position  $\vec{x}_i$ , and  $\vec{k}_i$  is the wave vector corresponding to the two-photon Raman transition for pulse  $i$ . The

inertial measurement sensitivity comes from the leading dependence of the phase shift on the local acceleration experienced by the atom, the Raman wave-vector and the time of flight:  $\Delta\Phi = \vec{k} \cdot \vec{a} T^2$ , where  $\vec{k}$  is the effective Raman wave vector,  $\vec{a}$  is the linear or Coriolis acceleration (' $a$ ' could for example, be  $g$ , the local gravitational acceleration or  $-2\vec{\Omega} \times \vec{v}$ , where  $\vec{\Omega}$  is the rotation rate and  $\vec{v}$  is the atom velocity in the case of the Coriolis acceleration), and  $T$  is the separation time between consecutive interferometer pulses. Figure 2 shows the coherent connection between the Raman atomic excitation, spatial recoil, and the space-time trajectories of the atoms in the interferometer.<sup>6</sup> Note that Coriolis acceleration depends on the sign of the velocity, but acceleration does not. This allows us to distinguish between rotation and linear acceleration by taking the sum or difference signals from two atom clouds launched in opposite directions.

For a gradiometer, where one is measuring the  $z$  (or  $x, y$ ) component of the gradient of the gravitational acceleration  $\nabla g$ , one has two vertically displaced laser-pulse atom accelerometers (see Figure 1) and the difference in the phase between the two gives the  $T_{zz}$  component (actually its finite difference analog) of the Cartesian gravity gradient tensor  $T_{ij} = \partial^2 U(\mathbf{r}) / \partial r_i \partial r_j$  ( $U(\mathbf{r})$  is the gravitational potential). Unlike the absolute value of the local acceleration, this tensor is insensitive to platform vibration noise and allows for measurement of gravitational anomalies such as those due to nearby, dense sources. This tensor data, then, is the input to our computational density distribution determination.

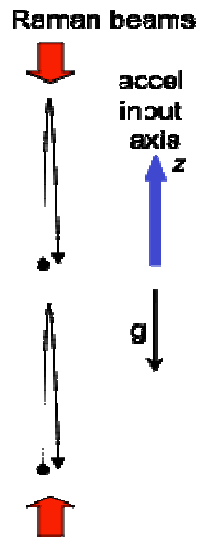


Figure 1. Cold atom  $T_{zz}$  gravity gradiometer (GG).

The relevant unit for gravity gradients is the ‘‘Eötvös’’ ( $1 \text{ E} = 10^{-9}/\text{s}^2$ ). For comparison, the gravity gradient of the Earth is  $\sim 3000 \text{ E}$ , a mass of  $75 \text{ kg}$  at distance of  $0.6 \text{ m}$  is  $8 \text{ E}$ , while an IAEA  $25 \text{ kg}$  sphere of highly enriched Uranium at a distance of  $1 \text{ m}$  creates a gradient of  $3.4 \text{ E}$ .

Assuming roughly white Allan phase noise sensitivity scaling we expect the mass detection threshold to vary as  $1/t^{1/2}$ . Because the sensor measures the field gradient, we can expect it to scale as  $1/r^3$  as a function of distance (or somewhat better when ‘close in’).

A cold atom  $T_{zz}$  gravity gradiometer (GG) consists of two vertically displaced interferometric accelerometers. Figure 1 shows the schematic for such a sensor, which has two regions for trapping and cooling atoms. Optical forces from the trapping lasers launch the atoms along a vertical trajectory. Figure 2 indicates the geometry of the atom launches, Raman beam laser-optic interaction, and the accelerometer measurements.

### **Comparison with other atom interferometric approaches**

Having already pointed out the clear advantages of cold atom based gradiometers to the mechanical alternatives, we now briefly compare the following different atom optic techniques<sup>6, 12</sup> that also might be applied to the passive detection of mass anomalies: 1) free-space optical gratings, 2) free-space mechanical gratings and 3) waveguides.

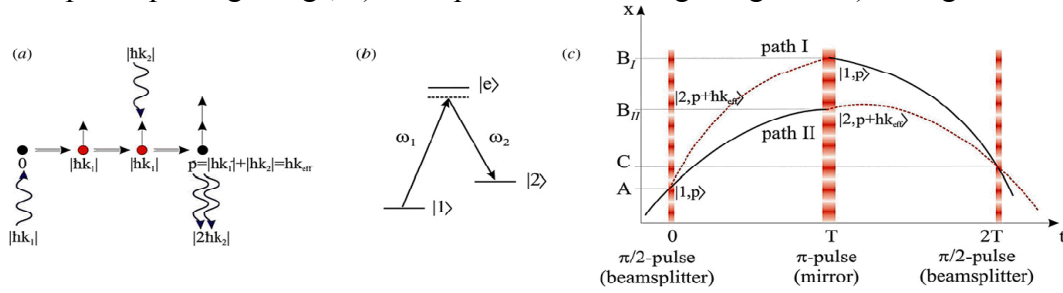


Figure 2. Atom interferometry based on Raman light pulses: (a) momentum transfer in a stimulated Raman transition; (b) simplified scheme of the atomic energy levels involved; (c) a Mach-Zehnder interferometer in spacetime plots: the atomic trajectories follow straight lines in the absence of gravity, and the parabolic curves in the presence of gravity.

*Free-space optical gratings (this work).* Pulses of light manipulate the cold atomic sources. The stability of the laser is used to manipulate the atomic wavepackets, guaranteeing sensor accuracy. The use of optical transitions, and in particular, two-photon stimulated Raman transitions, provides uniquely enabling capabilities for precision sensing: for example, electro-optic devices can dynamically shift the phase fronts of the optical fields, which allows sensors to simultaneously attain high dynamic range and high sensitivity.

*Free-space mechanical gratings.* Here microfabricated transmission/surface reflection gratings of  $\sim 100$  nm periodicity coherently diffract the de Broglie waves. It is unlikely a de Broglie wave sensor based on this technique can operate in highly dynamic environments, since gratings are subject to thermal and mechanical deformations. Additionally, the scale factor and bias offset will drift with temperature. These grating are mechanically delicate, and, in contrast with optical gratings, cannot readily be dynamically manipulated.

*Waveguides.* Unlike free-space sensors, here the atom is caged by a suitably strong confining potential, formed through optical potentials or magnetic fields. The accuracy is fundamentally tied to the dimensional stability and to the reproducibility of the waveguide geometry. It is therefore unlikely that this class of sensors will perform at levels surpassing existing mechanical or optical sensors, which are limited by similar

material considerations. For BEC-loaded waveguides, atom-atom collisions introduce nonlinearities that substantially complicate sensor properties. Finally, as atoms are caged to the sensor over the inertial measurement period, they are expected to be sensitive to high-frequency platform rotation and acceleration noise, and difficult-to-model force cross-couplings.

## Work performed under this LDRD Feasibility Study:

### *Computational models of the Interferometer/Gradiometer responses to test mass distribution.*

The 'imprinting' of the local gravitational field on each interferometer's cold atom entangled state trajectories driven by the launch, subsequent coherent beam splitting, recombining and readout, is the key to the sensor's performance. We therefore require an accurate model of the interferometer's phase shift as a function of the Earth's field and the perturbations due to local mass variations.

Generally speaking, the cold cesium atom's phase depends on the coherent dynamics of the effective Rabi oscillations of the two relevant hyperfine states ( $F=3, 4$ ) separated by about 9 GHz, the optical Raman pumped/feeder state (about 1 eV higher), and their correlation with the atom's momentum at each stage of the propagation in the interferometer.

In the case at hand, the atoms are launched at a time  $t = 0$ , undergo  $F=3, m_F=0$  state selection, and begin to decelerate under gravity. At some time  $t_0$ , the atoms are coherently

split into the  $F=3$  and  $F=4$  states by two counter-propagating lasers with a Rabi ' $\frac{\pi}{2}$ ' pulse.' This state splitting is accomplished by a nonlinear Raman process, which entangles the  $F=3$  and  $F=4$  states respectively with momenta differing by  $k_{eff} = |k_1| + |k_2|$ , where  $k_1$  and  $k_2$  are the wave vectors of the Raman light pulses and  $|k_1 - k_2|$  is proportional to the energy splitting between the hyperfine levels. The atoms, now entangled between two quantum states, after propagating for time  $T$ , are hit with a ' $\pi$  pulse,' reversing the atomic states, transferring momentum  $k_{eff}$  to the atoms previously in the  $F = 3$  state and  $-k_{eff}$  to those previously in  $F = 4$ . The momentum exchange drives the two different spatially coherent

portions of the atomic wave packet towards one another so that another ' $\pi$ ' pulse may recombine them at time  $t = t_0 + 2T$  (see Figure 3).<sup>1, 8, 12</sup>

The overall interferometer (semiclassical) phase is nominally composed of three parts: a small phase shift due to the finite ( $\sim 10 \mu s$ ) turn on of each Raman pulse, the free space propagation of the atoms between Raman pulses, and finally, the phase shift due to the Raman laser wavevector shift of the atom's momentum at the time of each pulse. Here, treating the Raman pulses as instantaneous, and working to order  $T^2$  in the pulse timing, we find that the phase shift is dominated by the successive interactions with the Raman pulses (equation 1). When the state of an atom is changed by a Raman pulse, it acquires an additional phase of  $\Delta\phi = \vec{k}_{eff} \cdot \vec{x}_p - \omega_{eff} t$  through the momentum transfer. Here,  $\vec{x}_p$  is the atom's position when struck by the pulse. Remarkably, the free space phase accumulation due to the propagation in the Earth's field cancels out.

$$1) \quad \Delta\phi_{laser} = \phi(\mathbf{x}^A, 0) - \phi(\mathbf{x}_1^B, T) - \phi(\mathbf{x}_u^B, T) + \phi(\mathbf{x}^C, 2T)$$

Therefore, the interferometer is sensitive to phase shifts that go as  $k_{\text{eff}} \delta x(t)$ , where  $\delta x(t)$  is the perturbation in the atomic position at time  $t$ . These phase shifts can be summed along both paths to find their final difference, essentially due to the Doppler shifts of the Raman wave vector along the component of the gravitational field  $g$ :

$$\phi_{ACB} - \phi_{ADB} = k_{\text{eff}} g T^2$$

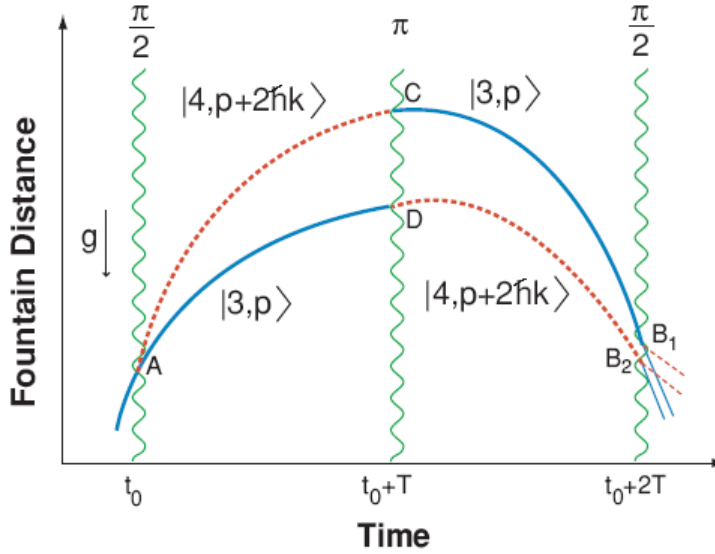


Figure 3

### Gravity Modeling

As already discussed in the introduction, the effect of interesting test masses on the trajectory of an interferometer atom, for any reasonable experimental setup, is small compared to that of the Earth. Therefore, the test mass's effect can be treated as a perturbation of Earth's gravity, i.e.:

$$\vec{z} = \vec{g}_0 + \delta \vec{g}$$

where  $g_0$  represents the Earth's gravitational acceleration, and  $\delta g$  the perturbation due to the test mass. Separating  $\vec{z}$  into components  $z$  and  $\delta z$ , due to the effects of Earth and the test mass on atomic position, allows for the isolation of the test mass's effect:

$$\delta \vec{z} = \delta \vec{g}(z)$$

Note that  $\delta g(z)$  is calculated using the unperturbed system's values:

$$\vec{z}(t) = \vec{z}_0 + \vec{v}_0 t + \frac{1}{2} \vec{g}_0 t^2$$

Using the acceleration Green's function  $|\vec{t} - \vec{t}'|$  the perturbation's effect on the atomic trajectory is:

$$2) \quad \delta \vec{z}(t) = \int_0^t dt' (t-t') \delta \vec{g}(\vec{z}(t'))$$

As discussed above, summing the test mass's effects at each of the Raman transition points yields its total contribution to an atom's trajectory in interferometers A & B due to the perturbation<sup>23</sup>:

$$3) \quad \delta z_{A,B}(t) = \delta z_{A,B}(t_0) - 2\delta z_{A,B}(t_0+T) + \delta z_{A,B}(t_0+2T)$$

Subtracting the individual interferometer shifts:  $\delta z_A - \delta z_B$ , dividing by  $T^2$  and the separation between the interferometers  $\delta z_{0A} - \delta z_{0B}$  then yields the gravity gradient in units of  $1/s^2$ .

$$\delta\phi = k_{eff} \cdot \left( \delta \vec{z}_A - \delta \vec{z}_B \right)$$

$$\text{Gravity Gradient} \sim \frac{\delta\phi}{k_{eff} T^2 (\delta z_{0A} - \delta z_{0B})}$$

The required vector perturbation  $\delta\vec{g}$  is given by the derivative of the source scalar potential. While we found it useful to apply analytic simplifications for the potentials due to specific symmetrical shapes such as spheres, cylinders, and cubes in order to check our results for the phase shifts, sufficiently accurate potentials for general mass distributions required the careful application of multipole expansions:

$$V(R, \theta, \Phi) = \sum_{l=0}^{\infty} \sqrt{\frac{4\pi}{2l+1}} \sum_{m=-l}^l \frac{Q_{lm}}{R^{l+1}} Y_{lm}^*(\theta, \Phi)$$

$$Q_{lm} = \int_V dV \rho(r', \theta, \phi) \sqrt{\frac{4\pi}{2l+1}} r'^l Y_{lm}(\theta, \phi)$$

where  $r', \theta$ , and  $\phi$ , are the coordinates of a source point. Furthermore, singularities in the time integral (eq. 2) for the overall phase shift require attention to spurious singularities in various nominally equivalent multipole forms. For example in the gradient

$$\frac{\partial(P_l(\cos(\theta)))}{\partial z}$$

, otherwise natural forms involving associated Legendre functions are problematic near  $z=0$ , while simple limits of polynomial combinations in the azimuthally symmetric body frame of the cylinder do the trick.

Because the multipole expansion, seen as a function of  $r'/R^{l+1}$ , converges rather slowly for our mass configurations of interest, it was necessary to include multipoles up to the 99<sup>th</sup> order in order to bound the resulting phase shifts to a part in  $10^{12}$ .

In order to model both earlier experiments and the background due to the containment box in the current work, it was also necessary to calculate the potential of a cubic mass. The potential at the atomic position  $(x_a, y_a, z_a)$  of a uniform parallelepiped of side lengths  $2a, 2b$ , and  $2c$  centered at the origin is:<sup>13</sup>

$$V(x_a, y_a, z_a) = \frac{Gm}{8abc} \int_{-a}^a du \int_{-b}^b dv \int_{-c}^c dw \frac{1}{\sqrt{[(x_a - u)]^2 + [(y_a - v)]^2 + [(z_a - w)]^2}}$$

A numerically smooth form for the gradient of  $V$  can be obtained via the chain rule with the quantity  $\partial V / \partial z_a$  becoming a double integral in  $u$  and  $v$  with a well-defined analytical form. Interestingly, for the case of a uniform cube, or, given superposition, a cubic shell, the potential is very close to a monopole source at the cube's center. The first correction,

which contributes a negligible amount to the phase shifts in this geometry, is a hexadecapole:  $\varphi \sim \frac{M}{r} + \mathcal{O}\left(\frac{1}{r^5}\right)$ .

As with rectilinear forms, analytically useful forms for cylinders<sup>21</sup> can also be obtained. In this case,

$$\Phi(r, z) = -2G\rho \int_0^h dz' \int_0^R dy \int_{-\sqrt{R^2-y^2}}^{\sqrt{R^2-y^2}} dx \frac{1}{\sqrt{y^2 + (x-r)^2 + (z-z')^2}}$$

with the radial and axial components of the acceleration given in terms of complete elliptic integrals<sup>22</sup>

$$a_r = 2G\rho f(r, \zeta) \Big|_{\zeta=z-h}^{\zeta=z},$$

via:

$$f(r, \zeta) = \int_0^R dy \ln \frac{\zeta + \sqrt{y^2 + \zeta^2 + [\sqrt{R^2 - y^2} + r]^2}}{\zeta + \sqrt{y^2 + \zeta^2 + [\sqrt{R^2 - y^2} - r]^2}} \text{ and}$$

$$a_z = 2G\rho f_z[(r, \zeta)] \Big|_{\zeta=z-h}^{\zeta=z},$$

$$f_z[(r, \zeta)] = g_+ - g_-,$$

$$g_{\pm} = \int_0^R dy \ln t(y)$$

$$t(y) = r \pm \sqrt{R^2 - y^2} + \sqrt{R^2 + r^2 + \zeta^2 \pm 2r\sqrt{R^2 - y^2}}$$

We anticipate that these forms (and the consequent interferometer phase shifts) will play a significant future role, not just in analytic checks of our data analysis, but in a gravity inversion code for mass determinations.

Armed with these analytic and numerical models, we computed predictions for a wide array of mass distribution ‘‘hypothesis’’ tests and compared them very successfully with experiment. Two examples, later dubbed cases A2 (left, and blue curve) & A3 (right, and red curve), are shown in Figure 4. As mentioned above, we also computed the background due to the aluminum containment box, its ‘foamular’ mass emplacement filling, and its support struts. This (shown in the experimental section), is case ‘‘EB’’ (empty box).

### ***Signal analysis***

While the specific signal analysis methods used in this study are detailed in the following section, we conclude this section on modeling with some remarks on ‘lock-in’ techniques, which, given the (ideal) Allan white phase noise characteristics of this type of sensor, are natural for future applications. The idea is to exploit the imposed periodicity (or known time history) of the physics signal to extract that signal from a noisy background. In particular, in this case, with the imposed mass translator ‘experimental

period'  $T_E$ , and the much longer overall data acquisition time  $T_M$ , one can extract the physics signal in the face of white noise, even when  $S/N < 1$ , by convolving the data time series with an appropriate function of period  $T_E$ . Stated in a Fourier basis, for a phase signal with (cosine) modes  $a_n$ , arbitrary overall temporal phase ambiguity  $\phi$ , and (white) noise modes  $b_n$  and  $c_n$ , the signal is:

$$\Delta\phi = \sum_n a_n \cos\left(\frac{2\pi n}{T_E}(t + \phi_{grad})\right) + \sum_n b_n \cos\left(\frac{2\pi n}{T_M}t\right) + \sum_n c_n \sin\left(\frac{2\pi n}{T_M}t\right)$$

$$T_E \ll T_M$$

Convolving this time series (e.g. to obtain the first cosine mode), with the lowest mode of period  $T_E$ , we obtain for  $a_1$ , (upon maximizing the convolution over  $\chi$ ), up to noise errors of order  $1/\sqrt{T_M}$ :

$$a_1\left(\frac{2\pi}{T_E}\right) = \frac{2}{T_M} \int_0^{T_M} dt (\Delta\phi \cos\left(\frac{2\pi}{T_E}(t + \chi)\right)) + \sqrt{T_M} O\left(\frac{1}{T_M}\right)$$

Though the lock-in method was quite useful in our analysis of earlier experimental data, in the present work, because of significant non-white 'technical' noise, we applied other decorrelation and averaging methods. In a future system, aimed at field operations, we will develop a synthesis of both types of data analysis.

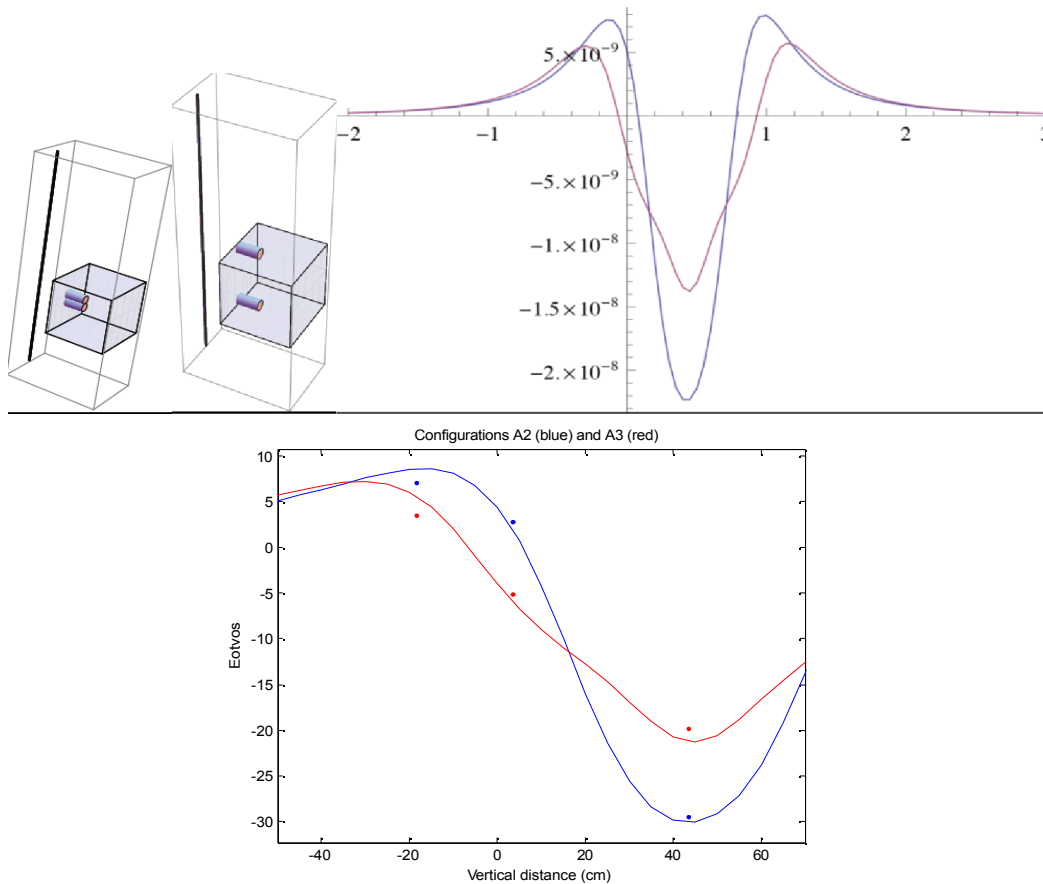


Figure 4. The top left diagram shows two mass configurations, A2 (cylinders together) and A3 (cylinders spaced). The top right plot shows simulations of A2 (blue) and A3 (red) as a function of

vertical distance in meters (x-axis). The y-axis is in units of  $1/s^2$ . The bottom plot also shows the simulations converted into Eötvös as a function of distance (cm), along with measurements (points).

### ***Hypothesis Testing Method:***

For the double blind experiments done as part of this project, and for future field applications of the mobile version of the sensor, we analyze the detection implications of the sensor data by pre-computing models of the sensor responses (theory + noise) the different mass distribution hypotheses as set of probability density functions. Assuming the outcomes for a given experimental situation for hypothesis “j” (same mass configurations, same time integration, etc.) are normally distributed (characterized by a mean outcome  $v_j$  and standard deviation  $\sigma_j$  coming from the underlying Allan noise analysis), we obtain relative probabilities for the different hypotheses after averaging N measurements. In particular, the relative probability for obtaining measurement x at given spatial position from the (hidden) hypothesized configuration j is:

$$P_j \sim \frac{e^{-N((x-v_j)/\sigma)^2}}{\sum_k e^{-N((x-v_k)/\sigma)^2}}$$

In this simplest version, where we assumed that all the  $\sigma_j$  are equal because they come from the same underlying sensor noise characteristics, the Gaussian normalizations divide out, leaving this simple form for  $P_j$ .

If we want to take into account the data for, say, three positions, the pdf for a given hypothesis returning a given set of three positional results is the product of the pdfs for each position. The overall relative probability is then the product for the hypothesis in question, divided by the sum of these products. If we want to include only a subset of the positional data, we correspondingly take only the corresponding pdfs in the products.

The hypothesis (j) with maximum likelihood value  $P_j$  is then chosen.

In the blind experiments done under this study, we assumed that the pdf’s for the different positions and mass configurations were independent (except for having the same noise controlled standard deviation). In fact, given the physics of the situation and different measurement protocols, there could be correlations due, for example, to the non-white Allan temporal correlations.

Acknowledgment:

Two of us (SBL and VS) would like to thank David Chambers for his statistical insights.

### ***Experimental Work***

*Background:*

The gravity gradiometer measures the population in each hyperfine state after passing through the interferometer. The normalized population difference (NPD) is related to the transition probability and is defined as the difference in state population divided by the total atom number, so the value can swing from -1 to 1 with 100% contrast. Plotting the NPD from the top interferometer vs. that from the bottom shows that measurements are confined to an ellipse even though spurious accelerations cause all angles around the

ellipse to be explored. This demonstrates the highly correlated signal between the interferometers and allows an ellipse fit to determine the relative phase.<sup>10</sup>

A commercial active vibration isolation platform can reduce environmental accelerations to  $\sim 25 \mu\text{gal} = 2.5 \times 10^{-7} \text{ m/s}^2$ , which is still too large to allow for the detection (in gravimeter mode) of small nearby masses relevant to emergency response. This drives us to work in gradiometer mode, where common vibrations are cancelled out, greatly increasing our sensitivity to small perturbing masses.

*Current work:*

The work under this feasibility study consists of operating the interferometer with fixed  $T$  and measuring the phase difference between the interferometers. Our goal is to show that the gradiometer is sensitive to differences in nearby mass distributions when the total mass is kept constant. To that end, it is required to sample a variety of locations around the mass distribution. A box containing various mass distributions is moved between three positions along the  $k_{\text{eff}}$  direction (vertical) near the sensor, as shown in Figure 5. Three positions were chosen as the minimum set required to differentiate the specific mass distributions used in this test, and the specific locations were chosen to maximize the differences in phase response between these mass distributions.

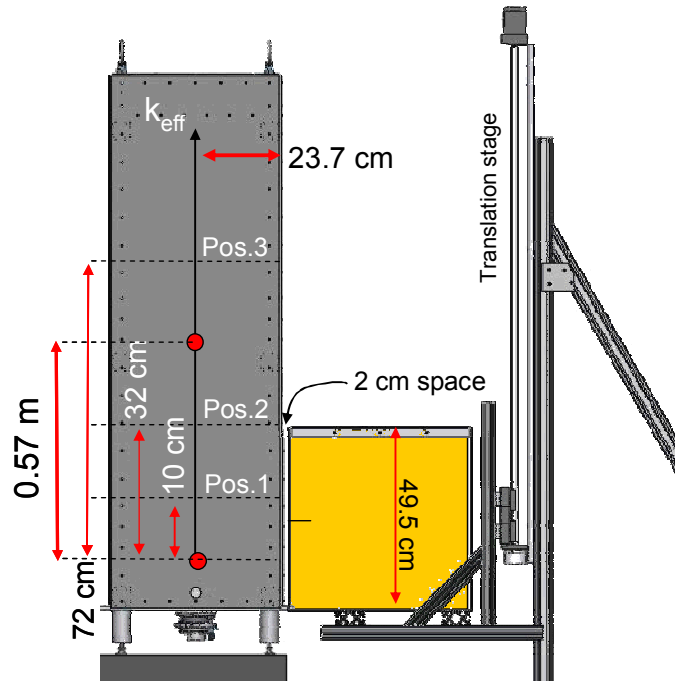


Figure 5. A schematic of the system is shown. The gravity gradiometer is on the left and has the launch direction and Raman beam direction labeled by the  $k_{\text{eff}}$  vector. Red circles separated by 0.57 m show the location of the atom launches for each interferometer. The three positions of the box (orange, 49.5 cm cube) containing masses are shown, and the box position is defined by the center in the vertical direction. The translation stage on the right runs at 1.7 cm/s. Some additional detail of the mass translation is shown in Figure 10.

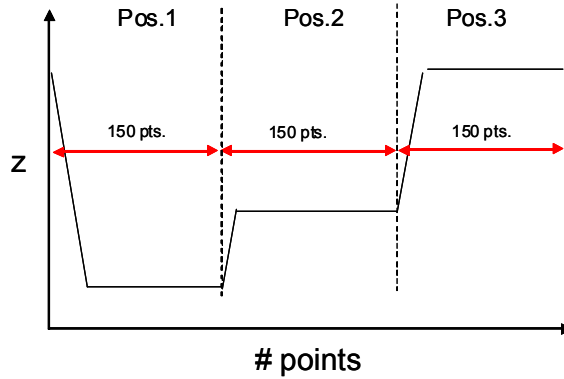


Figure 6. The vertical position ( $z$ ) as a function of data number (equivalent to time). For each 150 point window, the first section consists of translation to the location in that window. The time of translation is determined by the distance traveled divided by the fixed speed of 1.7 cm/s.

At each position the box is held for 150 measurements. This procedure is illustrated in Figure 6. A full cycle of the system contains 450 measurements (150 at 3 positions) and is repeated multiple times for each mass configuration. In these measurements only the relative phase difference is significant between box locations. This data collection method is different from the ellipse fitting described earlier, and has the advantage of higher data collection rate.

To extract the signal, repeated data is wrapped every 450 points and averaged to show the phase difference as a function of mass position. This is essentially the temporal behavior of the phase difference. Since there can be a long term drift in the phase difference, the data is either high pass filtered or, as is done in this case, the average value of each 450 point window is subtracted from that window. A more complete method of removing drifts consists of decorrelating the data with known environmental effects such as temperature and laser power. This was not implemented since the presence of large negative spikes in the relative phase when the box was triggered to move, which complicated this analysis by introducing effects we haven't previously quantified. We later learned that these spikes were caused by laser power drifts in different lasers associated with a software issue in triggering the translation of the box. A trivial solution is known.

The averaged value over the 150 points at each box position (neglecting the region of the spike) is compared to our predicted model in Figure 7. Since there is an overall phase ambiguity, the data is offset to minimize the squared difference between the data and model. Results from other mass configurations are shown at the end in Figure 9.

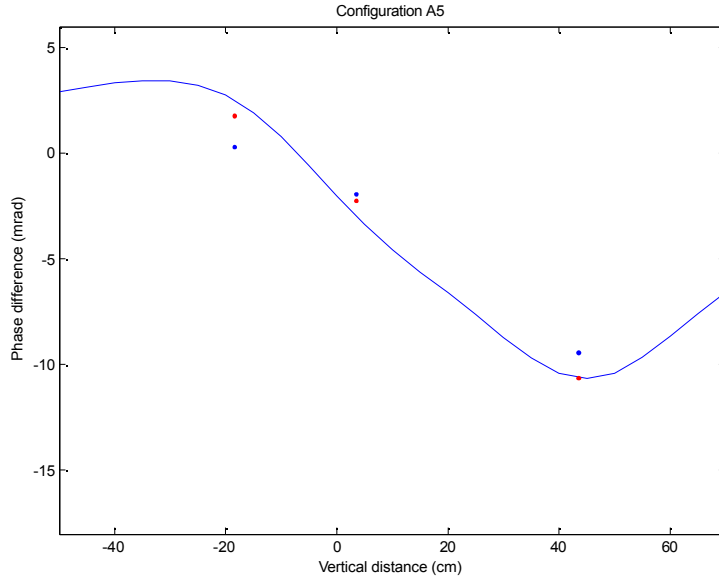


Figure 7. The averaged data from two measurements. The blue line is our model of the response for configuration A5 including a detailed model of the other moving hardware (box and support structure).

Measurement uncertainties (not shown in Figure 7) are determined by the number of points used in the average at each mass position and the characteristics of the noise. We usually classify noise sources as fundamental or technical. Fundamentally the atom interferometer's phase noise is white noise that scales like the square-root of the number of atoms, and averages down as  $1/\sqrt{t}$ . Technical noise sources can have a number of causes. Uncertainties were determined by using a long data set which included the software glitch from triggering the mass motion, but with the mass stationary. The error was read off the Allan deviation of that data set, based on the duration of each measurement.

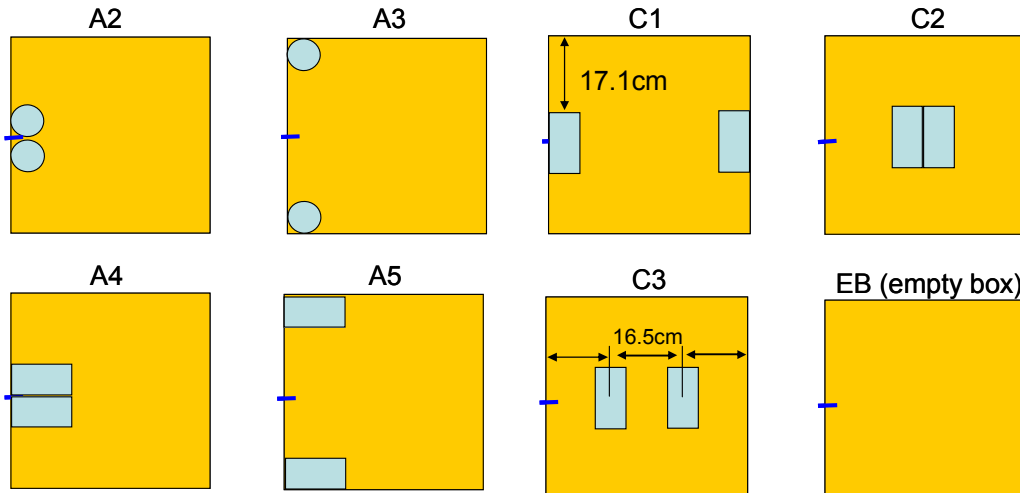


Figure 8. A summary of the mass configurations. The cylinders are solid tungsten with radius 7.30 cm and height 15.56 cm. Any dimensions not shown should be assumed to be symmetric in the box within 0.5 cm.

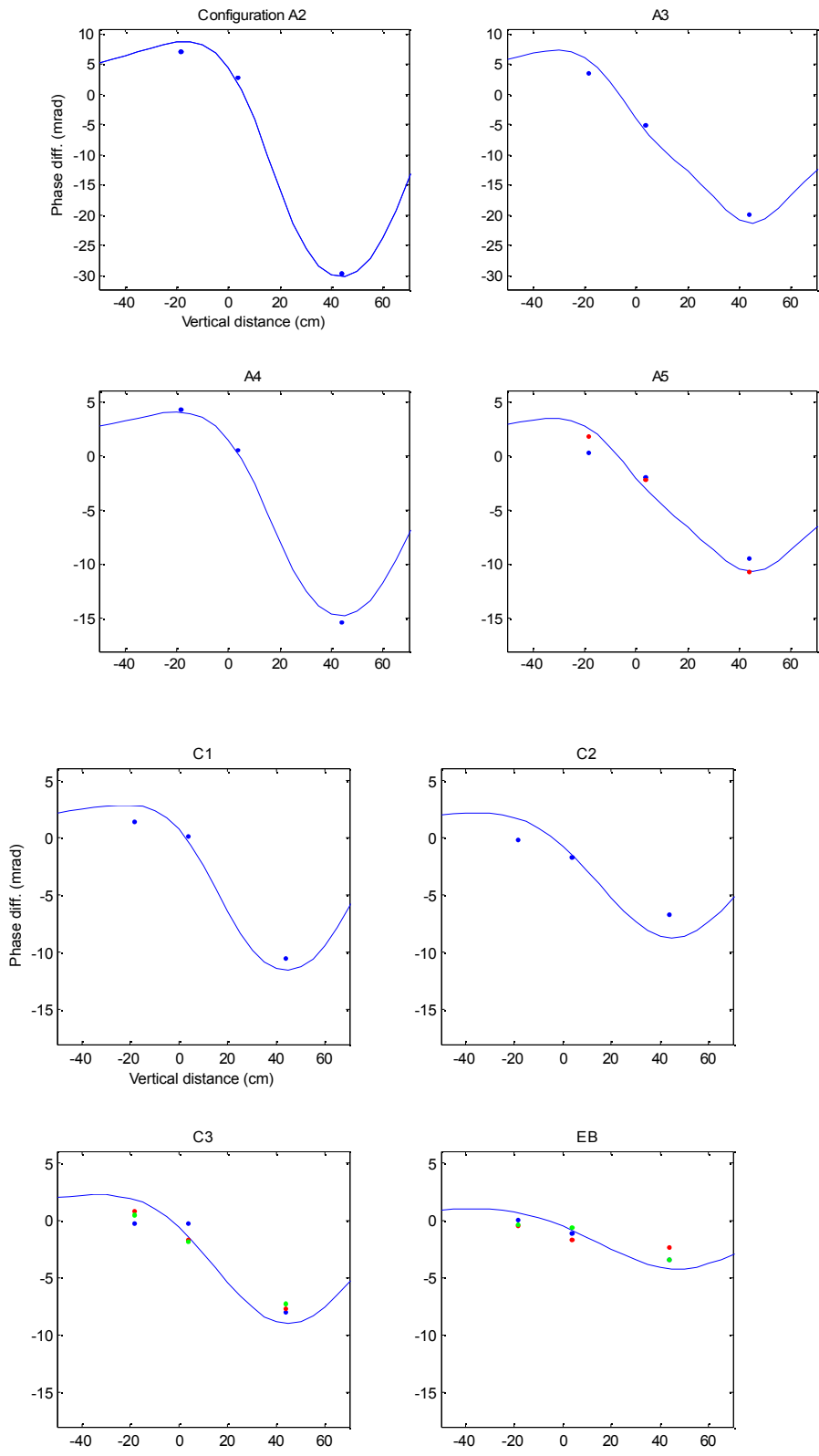


Figure 9. These plots show the results from measurements of the different mass distributions in Figure 8, showing excellent agreement with predictions. The vertical axis is the phase difference in mrad, and the

horizontal axis is the height in cm. Data sets C1, C2 and C3 were measured when the laser responsible for trapping, cooling, launching and detection was experiencing strong feedback from an optical isolator. This increased the detection noise and it is thought, increased the estimate of interference contrast, thereby decreasing the signal amplitude.

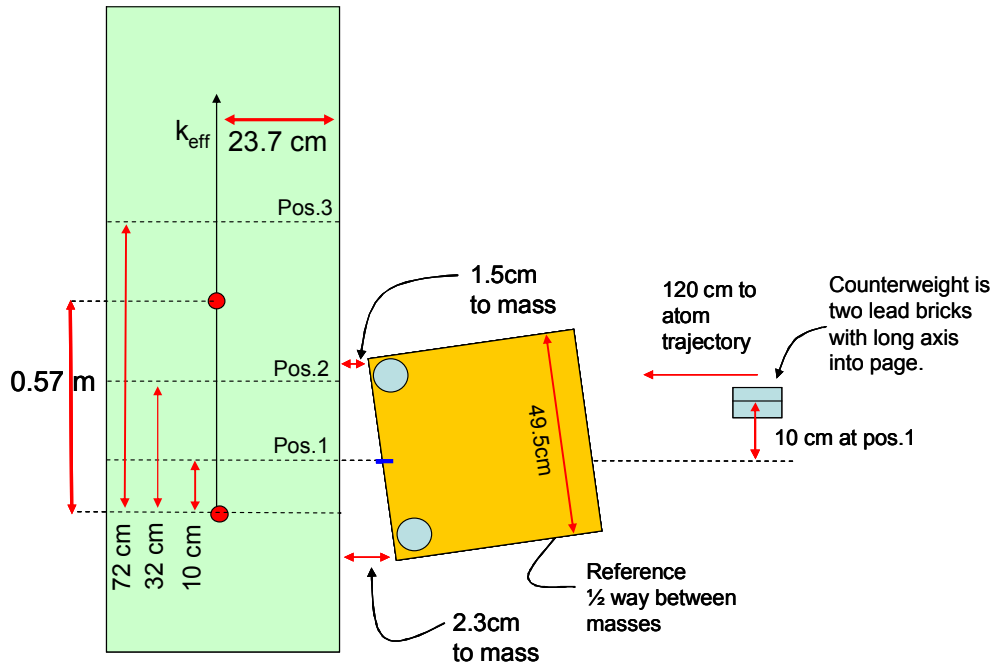


Figure 10. More detail of the mass system is shown, including a small tilt of the box, and a counterweight made of two 12 kg lead bricks which moves opposite of the box.

### Summary and Future Goals:

As can be seen in the results above (Figure 9), we successfully demonstrated the capability of this cold atom fountain gravity gradiometer to detect masses in the 10 kg range and distinguish their distributions (mainly quadrupolar variations) at distances of  $\sim 0.5$  m. We also developed (and experimentally validated) analytic and numerical models of the sensor response.

We have several clear goals for moving toward a mobile, passive, rapid response mass sensor for ER and treaty verification. These are as follows: 1 – design a miniaturized version of the sensor (this would likely parallel the AOSense efforts building a portable inertial motion sensor), 2 – model and carry out blind experiments with more ‘realistic’ mass distributions, 3 – apply our numerical sensor response models to the development of a full mass density inversion code<sup>20</sup> for field use, 4 – build and test in the field a prototype sensor.

Furthermore, we note that the AOSense gradiometer is correspondingly well suited to doing fundamental science gravitational measurements that will synergistically further

drive our mass imaging and signal analysis capabilities for ER. These experiments would be aimed at both making improved measurements of the gravitational coupling  $G$ , and at setting bounds on, or even discovering, new mass coupled interactions at the  $\sim$  centimeter length scale. (Earlier, superb work at the mm scale would be complemented by our effort.<sup>18, 19, 8</sup>) Our idea for these experiments is to exploit LLNL's unique imaging capabilities (for mass source characterization) and importantly, to recruit a strong post-doc from the cold-atom community who would work at LLNL and AOSense on the fundamental science experiments, but also to play a key role in the development and fielding of a prototype sensor in the ER community.

## References:

- <sup>1</sup>M. Kasevich and S. Chu, "Measurement of the gravitational acceleration of an atom with a light-pulse atom interferometer," *Appl. Phys. B* 54, 321 (1992). J. M. McGuirk, G. T. Foster, J. B. Fixler, M. J. Snadden and M. A. Kasevich, "Sensitive absolute-gravity gradiometry using atom interferometry," *Phys. Rev. A* 65, 033608 (2002).
- <sup>2</sup>T. L. Gustavson, P. Bouyer, and M. A. Kasevich, "Precision rotation measurements with an atom interferometer gyroscope," *Phys. Rev. Lett.* 78, 2046 (1997). T. L. Gustavson, A. Landragin and M. A. Kasevich, "Rotation sensing with a dual atom-interferometer Sagnac gyroscope," *Class. Quantum Grav.* 17, 2385 (2000). D. S. Durfee, Y. K. Shaham and M. A. Kasevich, "Long-term stability of an area-reversible atom-interferometer Sagnac gyroscope," *Phys. Rev. Lett.* 97, 240801 (2006).
- <sup>3</sup>J. B. Fixler, G. T. Foster, J. M. McGuirk and M. A. Kasevich, "Atom interferometer measurement of the Newtonian constant of gravity," *Science* 315, 74 (2007).
- <sup>4</sup>D. S. Weiss, B. C. Young and S. Chu, "Precision measurement of the photon recoil of an atom using atomic interferometry," *Phys. Rev. Lett.* 70, 2706 (1993). H. Müller, S.-W. Chiow, Q. Long, C. Vo and S. Chu, "A new photon recoil experiment: towards a determination of the fine structure constant," *Appl. Phys. B* 84, 633 (2006).
- <sup>5</sup>B. Young, K. Bongs, G. Biedermann, W. Li, J. Petricka, J. Fixler, Y. Shaham, G. Foster and M. Kasevich, "Atom interferometer-based inertial force sensors," presented at AIAA GNC 2002 (4-7 August 2002, Monterey).
- <sup>6</sup>M. de Angelis et. al., "Precision Gravimetry with atomic sensors," *Measurement Science and Technology* 20, 022001, (2009).
- <sup>7</sup>D. Allan, "Statistics of Atomic Frequency Standards," *Proceedings of IEEE*, Vol. 54, No 2, pp. 221–230, February 1966.
- <sup>8</sup>G. Biederman, "Gravity Tests, Differential Accelerometry and Interleaved Clocks with Cold Atom Interferometers," PhD dissertation., Stanford University, 2007.
- <sup>9</sup>S. Chu, L. Hollberg, J. E. Bjorkholm, A. Cable, A. Ashkin, "Three-Dimensional Viscous Confinement and Cooling of Atoms by Resonance Radiation Pressure," *Phys. Rev. Lett.*, Vol. 55, No. 1, pp. 48-51, 1985.
- <sup>10</sup>G. T. Foster, J. B. Fixler, J. M. McGuirk and M. A. Kasevich "Method of phase extraction between coupled atom interferometers using ellipse-specific fitting," *Optics Letters*, Vol. 27, No. 11, pp. 951-953, 2002.
- <sup>11</sup>S. B. Libby et. al., "Feasibility Study of a Passive, Stand-off Detector of High-Density Masses with a Gravity Gradiometer Based on Atom Interferometry," LLNL LDRD 10-FS-003, 2010.
- <sup>12</sup>A. Peters, K. Y. Chung, S. Chu, "High-precision gravity measurements using atom interferometry," *Metrologia*, Vol. 38, No. 1, pp. 25-63, 2001.
- <sup>13</sup>A. J. Swank, "Gravitational mass attraction: properties of a right-angled parallelepiped for the LISA drag-free system," *Classical and Quantum Gravity*, Vol. 23, No. 11, pp. 3437-3448, April 2006.
- <sup>14</sup>A. Romaides, J. C. Battis, R. W. Sands, A. Zorn, D. O. Benson, and D. J. DiFrancesco, "A Comparison of Gravimetric Techniques for Measuring Subsurface Void Signals," *J. Phys. D.: Appl. Phys.* **34** (2001), 433-443.
- <sup>15</sup>W. Telford, L. Geldart, R. E. Sheriff, and D. A. Keys, "Applied Geophysics," Cambridge University Press, 1990.

<sup>16</sup> S. D. Gray, J. A. Parmentola, and R. LeSchack, “Estimating the Weight of Very Heavy Objects with a Gravity Gradiometer,” *J. Appl. Phys. D* **28**, 2378, (1995).

<sup>17</sup> J. M. Goodkind, “The Superconducting Gravimeter,” *Rev. Sci. Instr.* **70**, 4131, (1999).

<sup>18</sup> M. V. Moody, H. J. Paik, “Gauss’s Law Test of Gravity at Short Range,” *Phys. Rev. Lett.* **70**, 1195, (1993)

<sup>19</sup> D. J. Kapner, T. S. Cook, E. G. Adelberger, J. H. Gundlach, B. R. Heckel, C. D. Hoyle, and H. E. Swanson, “Tests of the Gravitational Inverse-Square Law below the Dark-Energy Length Scale,” *Phys. Rev. Lett.* **98**, 021101, (2007), E. G. Adelberger, B. R. Heckel, et. al., “Particle-Physics Implications of a Recent Test of the Gravitational Inverse Square Law,” *Phys. Rev. Lett.* **98** 131104, (2007). C. D. Hoyle, D. J. Kapner, B. R. Heckel, E. G. Adelberger, J. H. Gundlach, U. Schmidt, and H. E. Swanson, “Submillimeter Tests of the Gravitational Inverse Square Law,” *Phys. Rev. D* **70**, 042004, (2004).

C. D. Hoyle, U. Schmidt, B. R. Heckel, E. G. Adelberger, J. H. Gundlach, D. J. Kapner, and H. E. Swanson, “Submillimeter Test of the Gravitational Inverse-Square Law, A Search for ‘Large’ Extra Dimensions,” *Phys. Rev. Lett* **86**, 1418, (2001). J. G. Wacker, “Using Atom Interferometry to Search for New Forces,” SLAC-PUB 13803, ArXiv:0908.2447v2.

S. Dimopoulos, P. W. Graham, J. M. Hogan, and M. A. Kasevich, “General Relativistic Effects in Atom Interferometry,” *Phys. Rev. D* **78**, 042002 (2008).

<sup>20</sup> B. Kirkendall, Y. Li, and D. Oldenburg, “Imaging Cargo Containers Using Gravity Gradiometry,” *IEEE Transactions on Geoscience and Remote Sensing*, **45**, 6, (2007), 1786. (this reference describes a density inversion code based on point gradiometric measurements. In contrast, the current sensor phase output measures the gravity gradient over the finite spatial extent of the atom trajectory in the interferometer.)

<sup>21</sup> A. H. Cook, and Y. T. Chen, *J. of Phys. A, Math. Gen.* **15**, 1591, (1982). Y. T. Chen, A. H. Cook, *Gravitational Experiments in the Laboratory*, Section 6.3, Cambridge University press, 1993.

<sup>22</sup> M. Abramowitz and I. A. Stegun, **Handbook of Mathematical Functions**, NBS, Washington, 1972.

<sup>23</sup> B. Dubetsky and M. A. Kasevich, *Phys. Rev. A* **74**, 023615 (2006).